

# Hopf solitons and knotted emergent fields in solid-state non-centrosymmetric magnets

Jung-Shen B. Tai (戴榮身)<sup>1</sup> and Ivan I. Smalyukh<sup>1,2,3\*</sup>

<sup>1</sup>Department of Physics, University of Colorado, Boulder, CO 80309, USA

<sup>2</sup>Materials Science and Engineering Program, Soft Materials Research Center and Department of Electrical, Computer and Energy Engineering, University of Colorado, Boulder, CO 80309, USA

<sup>3</sup>Renewable and Sustainable Energy Institute, National Renewable Energy Laboratory and University of Colorado, Boulder, CO 80309, USA

\*Corresponding author: [ivan.smalyukh@colorado.edu](mailto:ivan.smalyukh@colorado.edu)

*Abstract: Two-dimensional topological solitons, commonly called skyrmions, are extensively studied in solid-state magnets and promise many spintronics applications. However, their three-dimensional counterparts, dubbed hopfions, have not been demonstrated in these magnetic materials so far. Here we predict existence of such solitons with different Hopf index values in non-centrosymmetric solid magnetic nanostructures with perpendicular interfacial magnetic anisotropy. We show how this surface anisotropy, along with the Dzyaloshinskii-Moriya interactions and the geometry of nanostructures, enhances stability of hopfions. We demonstrate knots in emergent field lines and computer-simulate Lorentz transmission electron microscopy images of such solitonic configurations to guide their experimental discovery in magnetic solids.*

Topological solitons are widely studied in physical systems ranging from elementary particles to cosmology [1,2]. For example, Skyrme solitons in high energy physics [3] describe sub-atomic particles with different baryon numbers, which could be also obtained within an effective model of quantum chromodynamics [4]. A two-dimensional (2D) magnetic soliton described by elements of the second homotopy group,  $\pi_2(\mathbb{S}^2) = \mathbb{Z}$ , is a particle-like skyrmion with a localized winding of magnetization observed in non-centrosymmetric (chiral) magnets, of interest for

technological applications such as spintronics [5-7]. Hopfions are localized in all three spatial dimensions and classified on the basis of maps from  $\mathbb{R}^3 \cup \{\infty\} \cong \mathbb{S}^3$  to the ground-state manifold (target space)  $\mathbb{S}^2$  of three-dimensional unit vectors,  $\pi_3(\mathbb{S}^2) = \mathbb{Z}$ . Topologically distinct hopfions are characterized by the Hopf index  $Q \in \mathbb{Z}$  with a geometric interpretation of the linking number of any two closed-loop preimages, regions in space with the same orientation of field corresponding to a single point on  $\mathbb{S}^2$ . Hopfions were predicted to exist in many physical systems [1,2,8,9] and recently demonstrated as stable solitons in chiral colloidal ferromagnets through the direct 3D imaging and numerical simulations [10].

In this work, we theoretically predict stable static hopfions in non-centrosymmetric magnets with perpendicular magnetic anisotropy (PMA) at their interfaces. We show that, in addition to Dzyaloshinskii-Moriya interactions (DMI) [5], confinement and interfacial PMA help overcoming the constraints of Derrick theorem [11] by enhancing stability of solitonic configurations. We focus on fully non-singular field configurations, skyrmions and hopfions with different Hopf indices, and study knots in preimages and in emergent field associated with them; solitons accompanied by singular point defects (Bloch points), such as chiral bobbars [12] and torons [13], will be explored elsewhere. To facilitate experimental discovery of these structures, we construct diagrams of structural stability of localized field configurations versus material and geometric parameters and applied magnetic field. We also numerically simulate their Lorentz transmission electron microscopy (TEM) images and discuss how hopfions can be identified using real-space imaging techniques [6, 14, 15].

A computer simulated structure of magnetization field  $\mathbf{m}(\mathbf{r})$  of the Hopf soliton is shown in Fig. 1. It features closed-loop preimages corresponding to all points of  $\mathbb{S}^2$ , with each pair of distinct preimages linked the same  $Q$  number of times. The exterior of the torus-embedded region

is occupied by the preimage of the point in  $\mathbb{S}^2$  corresponding to the far-field background  $\mathbf{m}_0$  ( $+\hat{z}$ ), within which all other preimages are smoothly embedded (Fig. 1). Such elementary Hopf solitons comprise inter-linked closed-loops preimages of constant  $\mathbf{m}(\mathbf{r})$ , in this resembling the topology of mathematical Hopf fibration [16]. Due to the field topology, the emergent magnetic field  $(\mathbf{B}_{\text{em}})_i \equiv \hbar \varepsilon^{ijk} \mathbf{m} \cdot (\partial_j \mathbf{m} \times \partial_k \mathbf{m})/2$  [17-19] of a solid-state elementary hopfion spirals around its symmetry axis with a unit flux quantum [Fig. 1(c) & 1(d)]. Remarkably, each pair of streamlines of  $\mathbf{B}_{\text{em}}$  are linked exactly once and again resemble the Hopf fibration [16]. The emergent magnetic field describes the interaction between conduction electrons and the spin texture of the underlying solid, so that stabilized solid-state hopfions can lead to novel topological phenomena in quantum matter.

Overcoming constraints of the Derrick theorem [11], stability of Hopf solitons in chiral colloidal ferromagnets is enhanced by chirality (analogous to DMI) and typically strong perpendicular boundary conditions for  $\mathbf{m}(\mathbf{r})$  at confining surfaces [10], with the latter setting the uniform far-field background  $\mathbf{m}_0$ . In solid-state ferromagnets the surface interactions of  $\mathbf{m}(\mathbf{r})$  are weak and commonly neglected. However, strong effective interfacial PMA has been achieved on chiral magnet and Si interfaces due to magnetoelastic coupling [20, 21], on the magnetic metal and oxide interfaces [22], and in metallic multilayers [23], with reported values in the range of several  $\text{mJm}^{-2}$ . The role of effective PMA in chiral magnet/ferromagnet heterostructures was also studied [24]. These findings bring about the possibility of using surface confinement and boundary conditions to control stability of solitonic  $\mathbf{m}(\mathbf{r})$  structures, and below we show that interfacial PMA stabilizes a host of solitonic structures, including hopfions (Fig. 1).

We perform energy-minimizing routines on a micromagnetic Hamiltonian of an isotropic chiral magnet that contains both bulk and surface terms [25]

$$E = \int_{\Omega} d^3\mathbf{r} \left[ \frac{J}{2} (\nabla \mathbf{m})^2 + D \mathbf{m} \cdot (\nabla \times \mathbf{m}) - \mu_0 M_s m_z H \right] - \int_{\partial\Omega} d^2\mathbf{r} \frac{K_s}{2} (\mathbf{m} \cdot \mathbf{n})^2 \quad (1)$$

where  $J$  and  $D$  are Heisenberg exchange and DMI constants defining the helical wavelength  $\lambda = 2\pi(J/D)$ ,  $H$  and  $M_s$  are the magnetic field applied along  $\hat{z}$  and the saturated magnetization defining the Zeeman coupling energy,  $K_s$  characterizes the strength of PMA,  $\mathbf{n}$  is the easy-axis surface direction for  $\mathbf{m}(\mathbf{r})$  (chosen to be along the surface normal  $\hat{z}$ ),  $\Omega$  and  $\partial\Omega$  are the magnet's volume and boundary, respectively. The strength of PMA can be quantified by an extrapolation length  $\xi \equiv J/K_s$ , a virtual distance beyond the physical boundary where the hard boundary conditions are set, with  $\xi = 0$  for infinitely strong PMA. To make our finding relevant to different material systems, we scale length in units of  $\lambda$  and the magnetic field in units of  $H_D \equiv D^2/\mu_0 M_s J$ , the critical field strength for field-polarized state in bulk chiral magnet [26]. Computer simulations are performed for a series of hetero-structure geometries where chiral magnetic films of thickness  $d \sim \lambda$  are confined between thin (e.g. oxide) layers that define boundary conditions above and below the film, but not at its edges [Fig. 1(a)].

In nanodisks, ground-state hopfions with different Hopf indices (Fig. 2 and S1) arise from frustration that stems from competing terms in Eq. (1). The structural stability diagram also includes 2D skyrmions and topologically trivial helical, modulated helical and conical states (Fig. 2), though these structures and their energetic costs are also altered by the boundary conditions (supplementary Fig. S1). Elementary  $Q = 1$  hopfions are the ground state [Fig. 2(d)] at  $\xi/\lambda \lesssim 0.05$ ,  $D \gtrsim 2.8\lambda$  and  $H \lesssim 0.22H_D$ . Helical and 2D skyrmion states are hindered by high surface energy costs and exist only at large  $\xi$ , whereas conical and field-polarized states appear at large fields and for tight lateral confinement. Hopfions with  $Q = 2$  are stable at  $D \gtrsim 6\lambda$ , and future studies can explore how geometry of nanostructures can pre-define stability of hopfions with different  $Q$ . Supplementary Video S1 shows the structural evolution starting from a hopfion when

the boundary conditions are removed, demonstrating the role of PMA in hopfion stability. A “half-hopfion” structure, a 3D analog of the 2D meron, can be stabilized for asymmetric boundary conditions [Fig. 2(f-g)]. Free boundary conditions on the nanodisk edges result in the DMI-driven topologically trivial near-edge twist, consistent with the past studies of chiral magnetic nanostructures [27]. Computer-simulated Lorentz TEM images of a Hopf soliton for viewing directions along and perpendicular to  $\hat{z}$  are shown in Fig. 2(c) differ from 2D skyrmions and other solitonic structures, which may facilitate demonstration of hopfions in experiments.

Much like the skyrmionic A phase [28], hopfions can form a hexagonal 2D crystal in a film of thickness  $d$  (Fig. 3). In the film geometry, the translationally invariant conical state becomes the ground state while the hopfion crystal is metastable with its metastability dependent on  $H$ ,  $\xi$  and  $d$  (Fig. 2c). Hopfion stability is aided by strong boundary conditions at  $d \sim \lambda$ . At no fields, metastability conditions correspond to  $d/\lambda \gtrsim 0.85$  and  $\xi/\lambda < 0.056$ , equivalent to  $d \gtrsim 69$  nm and  $K_s > 1.6$  mJm<sup>-2</sup> for material parameters of FeGe (Table S1). Magnetic fields parallel to  $\mathbf{m}_0$  effectively aid in to the confinement and lower the interfacial PMA required for stability. However, these fields also promote formation of conical states and a larger  $d/\lambda$  is needed to gain stability by extra twisting. For example, hopfions can be metastable up to  $H = 0.3H_D$  at  $d/\lambda = 1.2$ , whereas magnetic fields antiparallel to  $\mathbf{m}_0$  raise the needed interfacial PMA and lower  $d/\lambda$ . Lorentz TEM images of a hexagonal hopfion crystal [Fig. 2(f)] differs from the images of hexagonal skyrmion crystals (see Refs. [6, 29] and computer simulated images in in Fig. S1 for comparison). Apart from the difference in pattern, the lattice constant is  $\sim \lambda$  in a skyrmion crystal [30, 31] and  $\gtrsim 2.5\lambda$  in a hopfion crystal. Hopfions also emerge in the channel geometries that can be used in the racetrack memory [7] and other spintronics applications (Fig. 4). Lorentz TEM images and  $\mathbf{m}(\mathbf{r})$  of these hopfions [Fig. 4(b)] qualitatively agree with the ones in films and nanodisks, though they

are asymmetrically squeezed due to the lateral confinement only in one direction. Interestingly, the difference between the hopfion crystal metastable state and the corresponding stable state is often  $<1\%$  of the equilibrium free energy, which means that the commonly neglected effects due to magnetostatic energy and various types of bulk anisotropy could bring about stability of 2D hopfion crystals in thin films and 3D hopfion crystals (and perhaps even quasicrystals) in bulk materials. Our findings call for a systematic study of various material parameters and confinement conditions under which such solitonic condensed matter phases could arise. Since hopfions of various  $Q$  can help embedding localized twisted regions of  $\mathbf{m}(\mathbf{r})$  in the uniform far-field ferromagnetic background, individual isolated hopfions could potentially arise during magnetic switching as transient or stable structures, though their stability in bulk materials remains an open question outside of the scope of present work.

Hopfions stabilized by fixed boundary conditions have their preimages closed and interlinked within the magnetic bulk [Fig. 1(b)]. The finite-strength interfacial PMA and the ensuing relaxed boundary condition allows the magnetization to deviate from  $\mathbf{m}_0$  at the surfaces. The largest deviation angle  $\theta_c$  defines a subspace of points with polar angles  $\theta < \theta_c$  on  $\mathbb{S}^2$  that have partially “virtual” preimages closed outside  $\Omega$  [Fig. 2(d) and 2(e)] but confined within the extended volume  $\Omega \cup \Omega'$  defined by the extrapolation length. At  $\xi = 0$ ,  $\theta_c = 0$  and  $\Omega' = 0$ , but both increase with  $\xi/\lambda$  until a threshold beyond which an abrupt transition to a structure without closed-loop preimages happens, making hopfions unstable. These hopfions can be analyzed by numerically integrating the Hopf index [32-35]:

$$Q = \frac{1}{64\pi^2} \int_{\Omega \cup \Omega'} d^3\mathbf{r} \epsilon^{ijk} A_i F_{jk}, \quad (2)$$

where  $F_{ij} = \varepsilon_{abc} m^a \partial_i m^b \partial_j m^c$ ,  $\varepsilon$  is the Levi-Civita totally antisymmetric tensor,  $A_j$  is defined as  $F_{ij} = (\partial_i A_j - \partial_j A_i)/2$ , and summation convention is assumed. For example, integration gives  $Q = 0.9997 \approx 1$  at  $d/\lambda = 0.85$  and  $\xi/\lambda = 0.056$ , consistent with  $Q = 1$  obtained from the geometric analysis of preimage linking.

To conclude, we predict ground-state and metastable hopfions in isotropic chiral magnets under nanoscale confinement of circular nanodisks, thin films and channels, including metastable hexagonal hopfion crystals in a thin film. Further extension of our model to include magnetostatic energy and bulk anisotropy terms can alter free energy landscape and be leveraged to further enhance stability of hopfions. We expect a wealth of fundamental phenomena in stable hopfions awaiting explorations, including their dynamics driven by spin transfer torques and the spiral emergent magnetic fields that form streamlines resembling Hopf fibration. Our work serves as a guide to their experimental discovery in solid-state materials. Furthermore, the capability of encoding 1, 0, and -1 and other states in the topological charges of 3D Hopf solitons in a chiral magnet can lead to new architectures of data storage devices and other spintronics applications.

We acknowledge discussions with P. Ackerman, A. Bogdanov, N. Nagaosa, Y. Tokura and H. Sohn and funding from the U.S. Department of Energy, Office of Basic Energy Sciences, Division of Materials Sciences and Engineering, under the Award ER46921. This work utilized the RMACC Summit supercomputer, which is supported by the National Science Foundation (awards ACI-1532235 and ACI-1532236), the University of Colorado Boulder and Colorado State University.

## Figures:

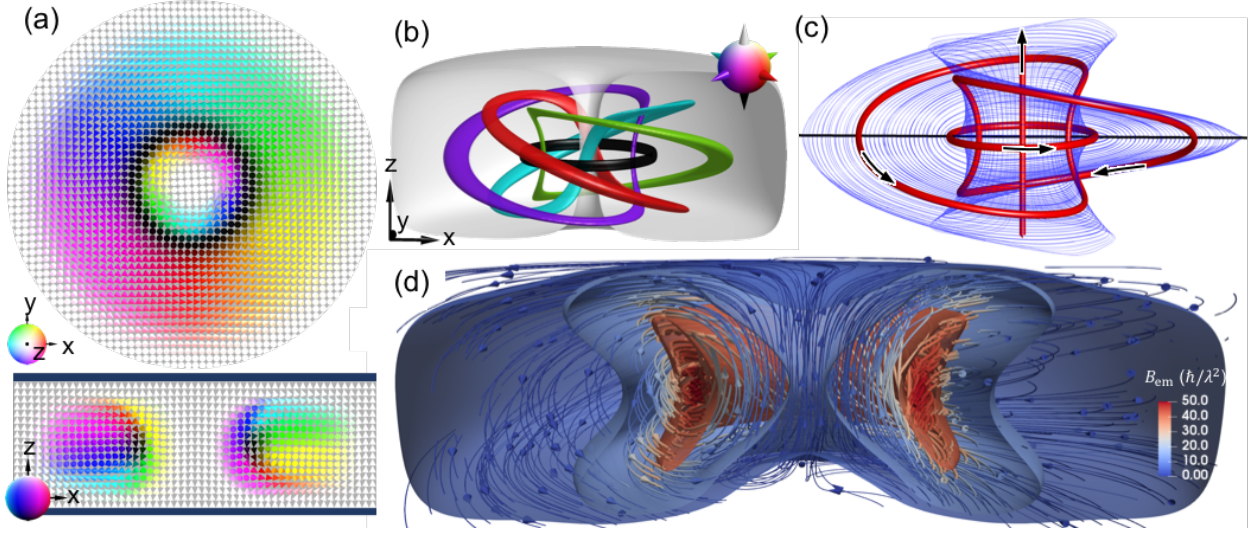


FIG. 1. 3D topological solution – hopfion. (a) Mid-plane cross-sections of a hopfion in the plane perpendicular to  $\mathbf{m}_0$  (upper) and in the vertical plane containing  $\mathbf{m}_0$  (lower). The magnetization fields are shown with cones colored according to the corresponding points on  $\mathbb{S}^2$  (lower-left insets). In the x-z cross-section, the black stripes at the top and bottom indicate fixed boundary conditions that can be achieved, for example, using thin films of a different material (e.g., oxide). (b) The 3D preimages of points on  $\mathbb{S}^2$  indicated as cones in the upper-right inset. The linking number of preimages yields  $Q = 1$ . (c) Streamlines of  $\mathbf{B}_{em}$  form the Hopf fibration. A subset of streamlines originating from points on a horizontal black line are illustrated by the blue lines, with some highlighted by red tubes to show interlinking of the ensuing closed loops, with the linking number 1. (d) Visualization of  $\mathbf{B}_{em}$  by the isosurfaces of constant magnitude and streamlines with cones indicating directions.



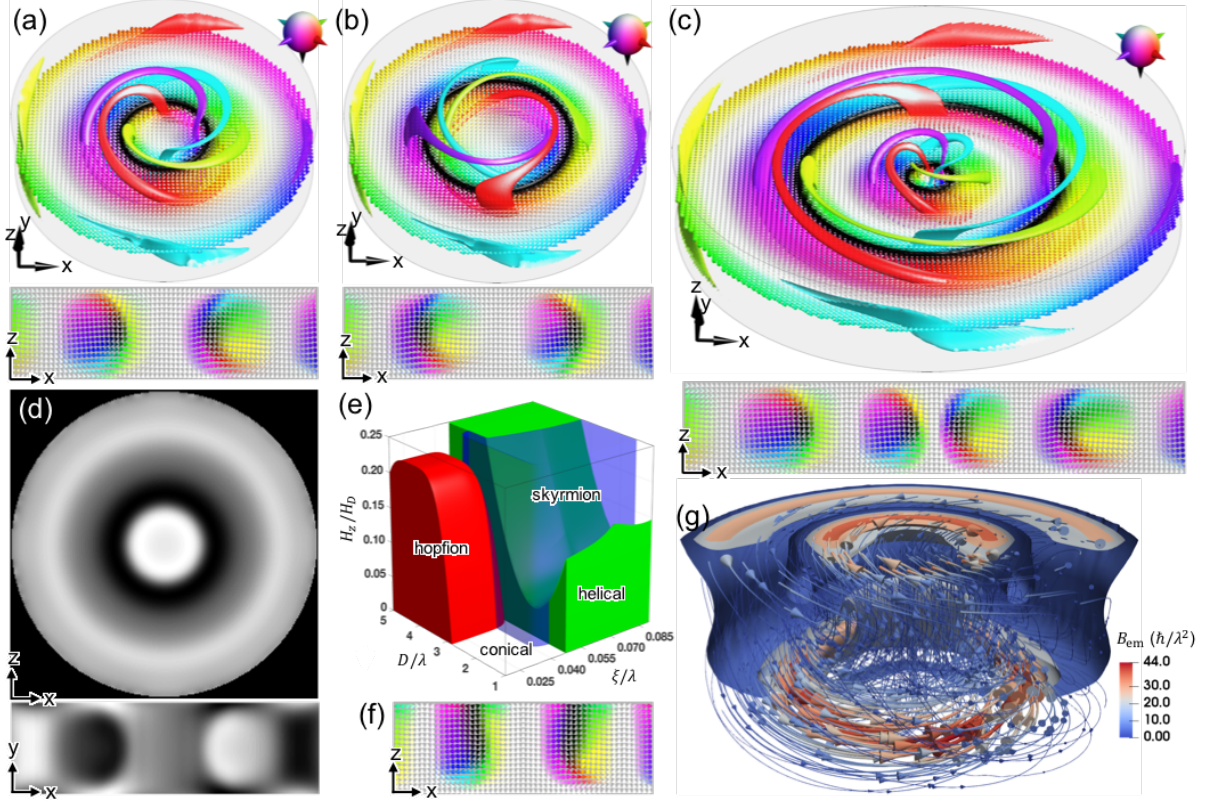


FIG. 2. Stable hopfions in circular nanodisks. (a, b, c) Horizontal mid-plane cross-sections (upper) and vertical mid-plane cross-sections (lower) of hopfions with  $Q = 1, -1$  and  $2$ , respectively, shown along with preimages of points on  $\mathbb{S}^2$  (corresponding to cones in the upper-right insets). (d) Computer-simulated Lorentz TEM images of a  $Q = 1$  hopfion shown in (a) for viewing directions along  $\hat{z}$  (upper) and perpendicular to it (lower). (e) Ground-state stability diagram of solitonic structures in nanodisks. The parameter space of stable hopfions, skyrmions and helical states are shown in red, blue and green, respectively, and that for the conical state is left blank. (f) A half-hopfion with PMA only on the bottom interface for  $d = 0.9\lambda$  and  $D = 4\lambda$ . (g) Visualization of half-hopfion's  $B_{em}$  derived from (f) by the isosurfaces colored by magnitude and streamlines with cones indicating directions.

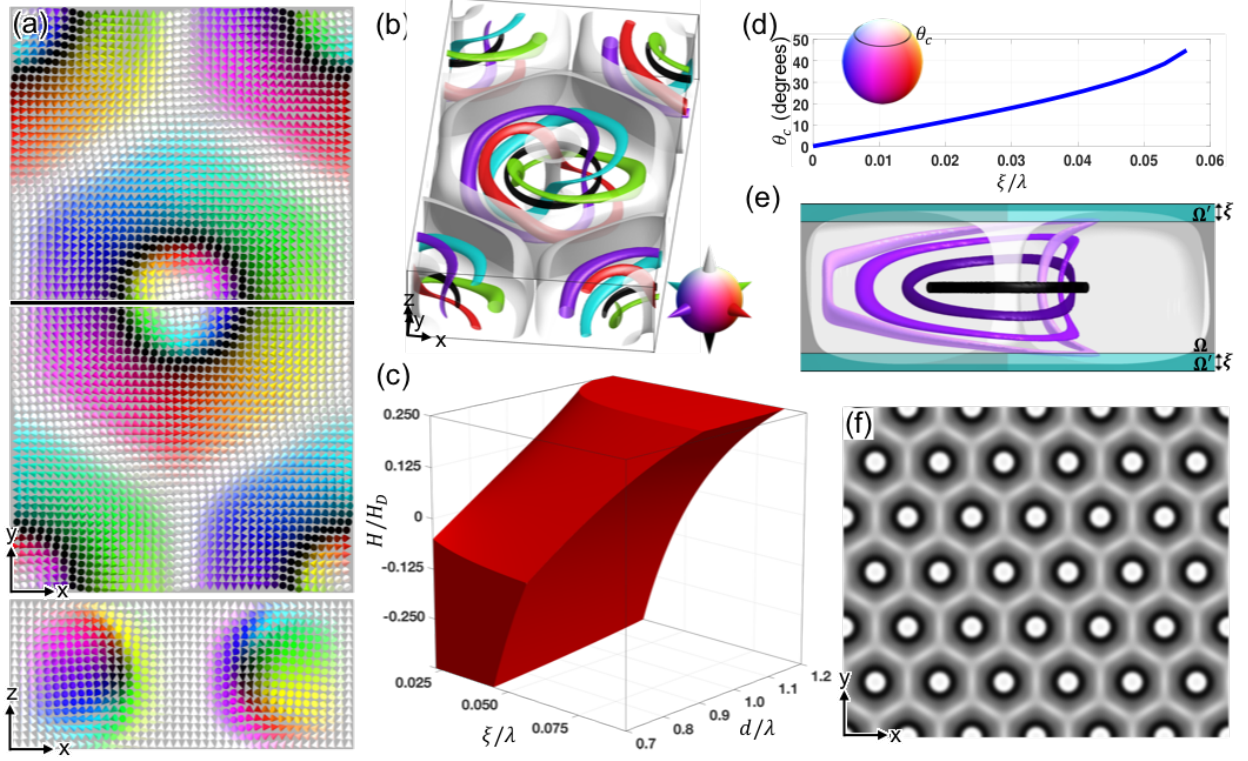


FIG. 3. Hexagonal hopfion crystal in a thin film of a chiral magnet. (a) Mid-plane cross-sections of a unit cell of the hopfion crystal in a plane perpendicular to  $\mathbf{m}_0$  (upper) and in the vertical plane (indicated by a black line in the upper panel) containing  $\mathbf{m}_0$  (lower). (b) 3D preimages of points on  $\mathbb{S}^2$  indicated by cones in the lower-right inset. (c) Diagram of metastability of a hopfion crystal (shown in red) vs.  $\xi/\lambda$ ,  $d/\lambda$  and  $H/H_D$ . (d) Dependence of  $\theta_c$  on  $\xi/\lambda$  at  $d/\lambda = 0.9$ . Shown in the inset is the target  $\mathbb{S}^2$  with the boundary at  $\theta = 45^\circ$  for  $\xi/\lambda = 0.056$ . (e) A unit cell of the hopfion crystal confined in the space  $\Omega \cup \Omega'$  extended by  $\xi$ . (f) A Lorentz TEM image of a 2D hopfion crystal.

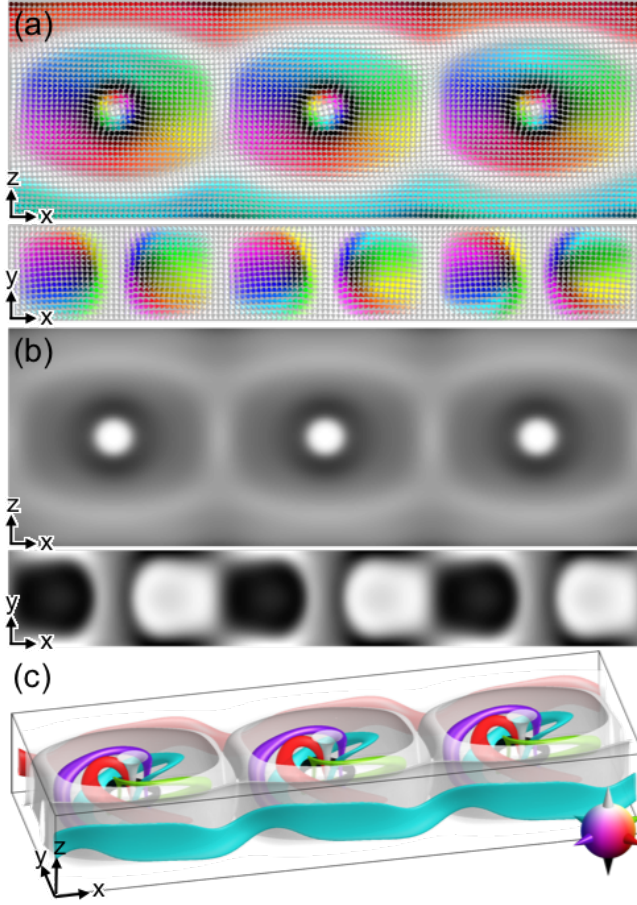


FIG. 4. Hopfions in magnetic channels shown for three unit cells. (a) Mid-plane cross-sections of a channel of hopfions in the plane perpendicular to  $\mathbf{m}_0$  (upper) and in the vertical plane containing  $\mathbf{m}_0$  (lower). (b) Computer-simulated Lorentz TEM images of hopfions in a channel when viewed along  $\hat{z}$  (upper) and orthogonally to it (lower). (c) 3D preimages of points on  $\mathbb{S}^2$  indicated as cones in the lower-right inset.

## References

1. N. Manton, P. Sutcliffe, *Topological Solitons* (Cambridge University Press, 2004).
2. L. Faddeev, A.J. Niemi, *Nature* **387**, 58 (1997).
3. T. H. R. Skyrme, *Proc. R. Soc. Lond. A* **260**, 127 (1961).
4. E. Witten, *Nucl. Phys. B* **223** 422 (1983).
5. A. Bogdanov, A. Hubert, *J. Magn. Magn. Mater.* **138**, 255 (1994);
6. X. Z. Yu, Y. Onose, N. Kanazawa, J. H. Park, J. H. Han, Y. Matsui, N. Nagaosa, Y. Tokura, *Nature* **465**, 901 (2010).
7. A. Fert, V. Cros, J. Sampaio, *Nat. Nanotechnol.* **8**, 152 (2013).
8. P. Sutcliffe, *Phys. Rev. Lett.* **118**, 247203 (2017).
9. J. H. Han, *Skyrmions in Condensed Matter* (Springer International Publishing AG, 2017)
10. P. J. Ackerman and I. I. Smalyukh, *Nat. Mater.* **16**, 426 (2017).
11. G.H. Derrick, *J. Math. Phys.* **5**, 1252 (1964).

12. F. Zheng et al., Nat. Nanotechnol. (2018) doi:10.1038/s41565-018-0093-3
13. I. I. Smalyukh, Y. Lansac, N. A. Clark, R. P. Trivedi, Nat. Mater. **9**, 139 (2010).
14. H. S. Park et al., Nature Nanotechnol. **9**, 337 (2014).
15. P. Milde et al., Science **340**, 1076 (2013).
16. H. Hopf, *Selecta Heinz Hopf* (Springer Berlin Heidelberg, German, 1964).
17. G. Volovik, J. Phys. C Solid State **20**, L83 (1987).
18. J. Zang, M. Mostovoy, J. H. Han, N. Nagaosa, Phys. Rev. Lett. **107**, 136804 (2011)
19. S. Zhang, S. S.-L. Zhang, Phys. Rev. Lett. **102**, 086601 (2009).
20. S. X. Huang and C. L. Chien, Phys. Rev. Lett. **108**, 267201 (2012)
21. E. A. Karhu, U. K. Roßler, A. N. Bogdanov, S. Kahwaji, B. J. Kirby, H. Fritzsche, M. D. Robertson, C. F. Majkrzak, and T. L. Monchesky, Phys. Rev. B **85**, 094429 (2012)
22. B. Dieny and M. Chshiev, Rev. Mod. Phys. **89**, 025008 (2017)
23. M. T. Johnson, P. J. H. Bloemen, F. J. A. den Broeder and J. J. de Vries, Rep. Prog. Phys. **59** 1409 (1996)
24. Y. Kawaguchi, Y. Tanaka, and N. Nagaosa, Phys. Rev. B **93**, 064416 (2016)
25. See Supplemental Material for details of numerical modeling of  $\mathbf{m}(\mathbf{r})$ .
26. A. Bogdanov, and A. Hubert, J. Magn. Magn. Mater. **138**, 255 (1994).
27. C. Jin et al., Nat. commun. **8**, 15569 (2017).
28. S. Mühlbauer, B. Binz, F. Jonietz, C. Pfleiderer, A. Rosch, A. Neubauer, R. Georgii and P. Böni, Science, **323**, 915 (2009).
29. X. Z. Yu, N. Kanazawa, Y. Onose, K. Kimoto, W. Z. Zhang, S. Ishiwata, Y. Matsui, and Y. Tokura, Nat. Mater. **10**, 106 (2011).
30. N. Nagaosa and Y. Tokura, Nat. Nanotechnol. **8**, 899 (2013).
31. K. Shibata, A. Kovács, N. S. Kiselev, N. Kanazawa, R. E. Dunin-Borkowski, and Y. Tokura, Phys. Rev. Lett. **118**, 087202 (2017)
32. J. H. C. Whitehead, Proc. Natl. Acad. Sci. U.S.A. **33**, 117 (1947)
33. P. Sutcliffe, Proc. Royal Soc. Lond. A **463**, 3001 (2007)
34. J. Hietarinta, J. Palmu, J. Jäykkä, P. Pakkanen, New J. Phys. **14**, 013013 (2012)
35. J.-S. B. Tai, P. J. Ackerman and I. I. Smalyukh, Proc. Natl. Acad. Sci. U.S.A. **115**, 921 (2018)



## Supplementary Figures & Tables

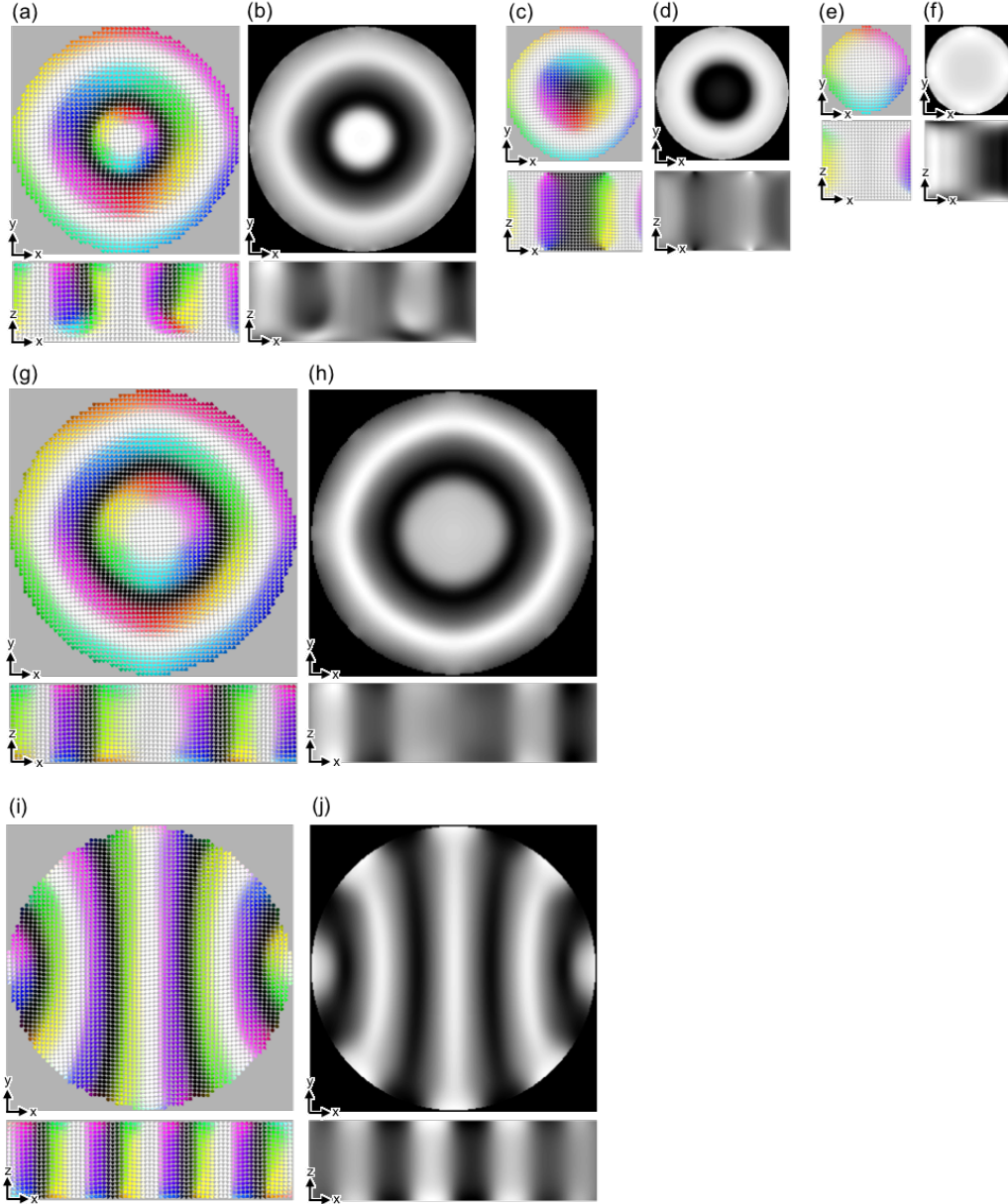


FIG. S1. Magnetization structures stabilized in circular nanodisks with  $d = \lambda$  of different diameters and boundary conditions (additional details for Fig. 2). (a, c, e, g and i) Mid-plane cross-sections of structures at no applied field in the plane perpendicular to  $\mathbf{m}_0$  (upper) and in the vertical plane containing  $\mathbf{m}_0$  (lower). (a) A half-hopfion obtained at  $D = 3.2\lambda$  and  $\xi/\lambda = 0.023$  on the bottom interface and no PMA on the top interface (c) A skyrmion obtained at  $D = 2\lambda$ ,  $\xi/\lambda = 0.045$  on both interfaces. (e) An (axially-symmetric) conical state obtained at  $D = 1.33\lambda$  and  $\xi/\lambda = 0.045$  on both interfaces. (g) A modulated helical state (skyrmion-antiskyrmion pair) that appears as a result of a hopfion transformation upon switching PMA off at  $D = 4\lambda$ . (i) A helical state obtained at  $D = 4\lambda$  and no PMA on either interface. (b, d, f, h and j) Computer-

simulated Lorentz TEM images of structures corresponding to (a, c, e, g and i), respectively, when viewed along  $\hat{z}$  (upper) and along  $\hat{y}$  (lower).

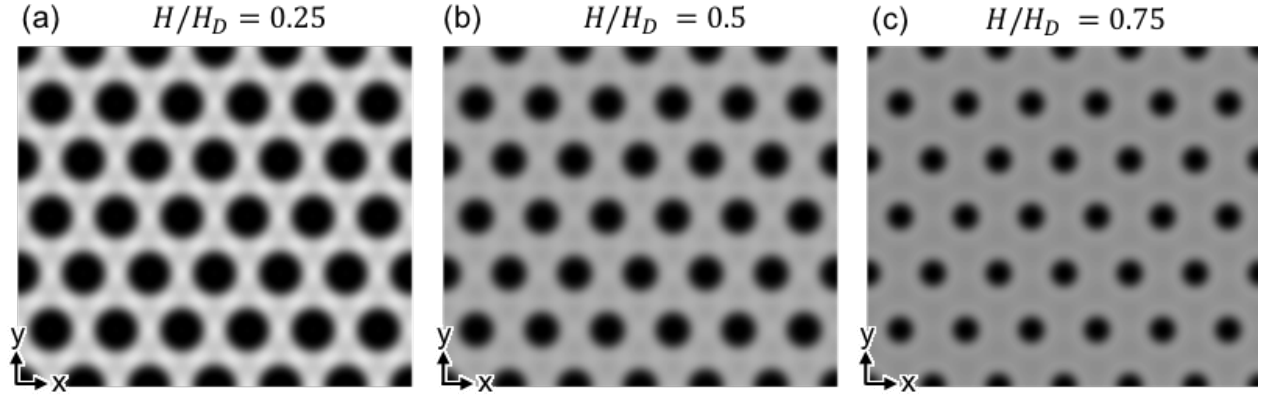


FIG. S2. Computer-simulated Lorentz TEM images of a 2D skyrmion crystal at different applied magnetic fields.

Table S1. Material parameters of FeGe at 200K [1].

| $J$                     | $D$                     | $\lambda = 2\pi(\frac{J}{D})$ | $\mu_0 M_s$ |
|-------------------------|-------------------------|-------------------------------|-------------|
| 7.290 pJm <sup>-1</sup> | 0.567 mJm <sup>-2</sup> | 80.8 nm                       | 0.14T       |

## Supplementary Methods

In the continuum approximation, the effective Hamiltonian of an isotropic bulk chiral magnet is given by the volume integral in Eq. (S1)

$$E = \int_{\Omega} d^3\mathbf{r} h = \int_{\Omega} d^3\mathbf{r} \left[ \frac{J}{2} (\nabla \mathbf{m})^2 + D \mathbf{m} \cdot (\nabla \times \mathbf{m}) - \mu_0 M_s \mathbf{m} \cdot \mathbf{H} \right] \quad (\text{S1})$$

where  $J$  and  $D$  describe the magnitude of Heisenberg exchange and the Dzyaloshinskii-Moriya interaction (DMI) and the resulting helical wavelength is  $\lambda = 2\pi(J/D)$ . The last term in Eq. (S1) is the Zeeman energy density describing the coupling between the magnetization and the applied magnetic field  $\mathbf{H}$ , where  $M_s$  is the saturated magnetization. When taking into account magnetic anisotropy energy on the boundaries, Eq. (S1) is supplemented with a surface term

$$- \int_{\partial\Omega} d^2\mathbf{r} \frac{K_s}{2} (\mathbf{m} \cdot \mathbf{n})^2 \quad (\text{S2})$$

where  $K_s$  characterizes the strength of the interfacial magnetic anisotropy and  $\mathbf{n}$  is the easy-axis direction for  $\mathbf{m}(\mathbf{r})$ .

For the static field configurations to be observed in the magnetic system, they need to emerge as local or global minima of the Hamiltonian given by Eqs. (S1) and (S2). Numerical modeling of the energy minimization of  $\mathbf{m}(\mathbf{r})$  is performed by a variational-method-based relaxation routine which also includes the boundary effects [2-4]. After discretizing the computational volume, each node is identified to be either a bulk node or a boundary node. At each iteration of the numerical simulation,  $\mathbf{m}(\mathbf{r})$  is updated based on an update formula derived from the Lagrange equation of the system,

$$m_i^{\text{new}} = m_i^{\text{old}} - \frac{\text{MSTS}}{2} [E]_{m_i} \quad (\text{S3})$$

where the subscript  $i$  denotes spatial coordinates,  $[E]_{m_i}$  denotes the functional derivative of  $H$  with respect to  $m_i$ . To include the boundary effects,  $[E]_{m_i}$  at a boundary node takes a different form than at a bulk node. Specifically

$$[E]_{m_i} = \frac{\partial h}{\partial m_i} - \nabla \cdot \frac{\partial h}{\partial \nabla m_i} \quad (\text{bulk}) \quad (\text{S4})$$

$$[E]_{m_i} = \frac{\partial h}{\partial \nabla m_i} \cdot \hat{\mathbf{e}} - K_s(\mathbf{m} \cdot \mathbf{n})n_i \quad (\text{boundary}) \quad (\text{S5})$$

where  $\hat{\mathbf{e}}$  is the surface normal on the boundary. MSTs is the maximum stable time step in the minimization routine, determined by the values of material parameters and the spacing of the computational grid [2-4]. The steady-state stopping condition is determined by monitoring the change in the spatially averaged functional derivatives over iterations. When this value approaches zero, the system is implied to be in a state corresponding to the energy minimum, and the relaxation routine is terminated. By iteratively solving the Euler-Lagrange equation derived from Eqs. (S1) and (S2), energy minima and evolution dynamics of the magnetization  $\mathbf{m}(\mathbf{r})$  can be found.

The 3D spatial discretization is performed on large 3D square-periodic grids with 24 to 72 grid points per helical wavelength  $\lambda$ . The spatial derivatives are calculated by finite difference methods with second-order accuracies based on central difference for the bulk nodes and one-sided differences for the boundary nodes, respectively, allowing us to minimize discretization-related artifacts. For simulating hexagonal hopfion crystals, periodic boundary conditions are imposed in both lateral directions. Periodic boundary conditions are imposed along one direction in the case of hopfions in channels. Both the analytical ansatz configurations [5,6] and manipulations of the stabilized configurations of the analytical ansatz are used as initial conditions.



To construct a preimage of a point on  $\mathbb{S}^2$  within the 3D volume of the static topological solitons, we calculate a scalar field defined as the difference between the magnetization field  $\mathbf{m}(\mathbf{r})$  and a unit vector defined by the target point on  $\mathbb{S}^2$ . The preimage is then visualized with the help of the isosurfaces of a small value in this ensuing scalar field. The Hopf index  $Q$  of a 3D topological soliton can be geometrically interpreted as the linking number of each pair of distinct preimages [5]. By choosing the circulation of the preimage of the north pole on  $\mathbb{S}^2$  to be along  $\mathbf{m}_0$  through the center of the topological solitons, the circulations of all other preimages are determined by smoothly moving away from the north pole and exploring  $\mathbb{S}^2$ . Note this choice does not affect the resulting linking number. The linking number of preimages is then defined as half the total number of crossings, with the sign of each crossing defined by the convention based on the right-hand rule [5,7]. Within this procedure, by flattening the right hand, we extend the fingers in the direction along the circulation of one preimage with the palm facing the other. The sign of the crossing is then positive if the circulation of the other preimage and the thumb's direction point toward the same side with respect to the first preimage, and negative otherwise. The values of  $Q$  determined via this approach is consistent with the one obtained via numerical integration, as described below.

To numerically calculate the Hopf index by integrating Eq. (2) in the main text, we can define  $b^i \equiv \varepsilon^{ijk} F_{jk}$  such that  $b^i = \varepsilon^{ijk} (\partial_j A_k - \partial_k A_j)/2 = \varepsilon^{ijk} \partial_j A_k$  and  $\mathbf{A}$  can be understood as the vector potential of the vector field  $\mathbf{b}$ , and  $Q$  can be rewritten as  $Q = 1/64\pi^2 \int d^3\mathbf{r} \mathbf{b} \cdot \mathbf{A}$ . After calculating  $\mathbf{b}$  from  $\mathbf{m}(\mathbf{r})$ , the vector potential  $\mathbf{A}$  can be obtained by numerically integrating  $\mathbf{b}$  [7]. The numerically integrated  $Q$  approaches that determined geometrically by the linking number of preimages as the solitonic field configurations are interpolated on a finer grid. In this work, the

fields were interpolated on a grid 8 times finer than the original grid, for which the free-energy minimization was performed.

To simulate Fresnel mode images of Lorentz transmission electron microscopy, we make use of the following equation, which describes the intensity of an image at small defocus  $\Delta$  for a thin film normal to the electron beam direction  $\hat{\mathbf{l}}$  [8]

$$I(\mathbf{r}) = 1 - \int_0^d dl \Delta \frac{e\mu_0\lambda_e}{h} (\nabla \times \mathbf{m}(\mathbf{r})) \cdot \hat{\mathbf{l}} \quad (\text{S6})$$

where  $\lambda_e$  is the electron wavelength,  $d$  is the film thickness, and  $e$ ,  $\mu_0$  and  $h$  are the electron charge, vacuum permeability, and the Planck constant, respectively. The contrast of each image is then normalized.

#### Supplementary References:

1. R. Takagi et al., Phys. Rev. B **95** 220406 (2017).
2. P. J. Ackerman and I. I. Smalyukh, Nat. Mater. **16**, 426-432 (2017).
3. P. J. Ackerman and I. I. Smalyukh, Phys. Rev. X **7**, 011006 (2017).
4. M. Ravnik, and S. Žumer, Liquid Crystals **36**, 1201 (2009).
5. N. Manton and P. Sutcliffe, *Topological Solitons* (Cambridge University Press, 2004).
6. J. Hietarinta, J. Palmu, J. Jäykkä, P. Pakkanen, New J. Phys. **14**, 013013 (2012).
7. J.-S. B. Tai, P. J. Ackerman and I. I. Smalyukh, Proc. Natl. Acad. Sci. U.S.A. **115**, 921 (2018)
8. S. McVitie, and M. Cushley, Ultramicroscopy **106**, 423 (2006).